Article

Smart Combination of Cyclodextrin Polymer Host-Guest Recognition and Mg-Assistant Cyclic Cleavage Reaction for Sensitive Electrochemical Assay of Nucleic Acids

Jingjing Jiang, Xinyi Lin, and Guowang Diao

ACS Appl. Mater. Interfaces, **Just Accepted Manuscript** • DOI: 10.1021/acsami.7b13132 • Publication Date (Web): 06 Oct 2017

Smart Combination of Cyclodextrin Polymer Host-Guest Recognition and Mg^{2+}-Assistant Cyclic Cleavage Reaction for Sensitive Electrochemical Assay of Nucleic Acids

Jingjing Jiang, Xinyi Lin, and Guowang Diao*

School of Chemistry and Chemical Engineering, Yangzhou University, Yangzhou 225002, PR China

ABSTRACT

A novel enzyme-free electrochemical sensing strategy was proposed for sensitive monitoring of DNA and miRNA by smart combination of the cyclic cleavage reaction of Mg^{2+}-dependent DNAzyme and the host-guest inclusion between ferrocene-labeled hairpin probe (H-1) and nitrogen-doped reduced graphene oxide/β-cyclodextrin polymer (NRGO/β-CDP) nanocomposites. The synthesized NRGO/β-CDP nanocomposites with high electrocatalytic activity and recognition capability were modified on the glassy carbon electrode to construct the sensing platform. Upon the hybridization reaction of subunit DNA in the loop region with target sequence, the active DNAzyme was liberated from the caged structure, which bound with H-1 to catalyze its cleavage in the presence of Mg^{2+} and triggered the target recycling amplification for the cleavage of a large number of H-1. Each cleaved H-1 was divided into two single-stranded oligonucleotides, leading to an obvious enhancement of peak current by the molecular recognition of β-CDP on the electrode. Thus, the constructed biosensor showed high sensitivity and selectivity for DNA and miRNA assays, with wide concentration ranges of 0.01−1000 and 0.05−500 pM, low detection limits of 3.2 and 18 fM, respectively. This developed sensing strategy may become a promising nucleic acid detection method in bioassays and clinical diagnosis.

KEYWORDS: Nitrogen-doped reduced graphene oxide; β-Cyclodextrin polymer; DNAzyme; Biosensor; Electrochemical detection

* Corresponding author. E-mail address: gwdiao@yzu.edu.cn

■INTRODUCTION

Carbon-based nanostructured materials, especially graphene has gained extensive attention in bioelectronics and biosensing, because of its unique properties, including huge surface area, superior electronic conductivity, and good chemical durability.[1–3] Recent researches have proved that chemical doping with heteroatoms (e.g. boron and nitrogen) as a powerful method can effectively modulate the electronic properties, surface and local chemical features of graphene.[4,5] It is worthwhile to develop metal-free or non-precious metal electrocatalysts with desirable catalytic performances for novel device applications.[6,7] The lone-pair electrons of nitrogen atoms can generate delocalized conjugated systems with the sp^2-hybridized carbon frameworks,[8,9] resulting in the considerable improvement of electrocatalytic property of nitrogen-doped graphene for the oxygen reduction reaction in fuel cells. However, the low solubility of graphene and heteroatoms-doped graphene in water extremely affects their performances in practical applications.[10,11] To overcome this obstacle, covalent[12–14] or noncovalent[15–17] approaches were successfully applied to ameliorate the dispersing and stability of these carbon nanomaterials in aqueous media.

Cyclodextrins (CDs) are a series of cyclic oligosaccharides consisting of six, seven, or eight glucose units (α-, β-, or γ-CD, respectively), creating a truncated cone shape with a hydrophilic external surface to provide water solubility and a hydrophobic internal cavity for host-guest recognition.[18,19] Recent reports have indicated that β-CD could be adsorbed on carbon materials (e.g. graphene and carbon nanotubes) to produce water-soluble nanocomposites through the hydrogen bonding, van der Waals

force, and hydrophobic interaction.[20,21] In comparison with β-CD, β-cyclodextrin polymer (β-CDP) which was generated by the cross-linking reaction between β-CD and epichlorohydrin (EP),[22] exhibited higher water solubility and stronger recognition capability toward guest molecules.[23] On the basis of the integration of nitrogen-doped reduced graphene oxide (NRGO) and β-CDP, the resultant nanocomposites could combine the unique properties of NRGO (superior electrocatalytic activity) and β-CDP (high water solubility and recognition capability), and have promising applications in the fields of electronics, sensors, and electrocatalysis.

Owing to the ever increasing requirements of highly sensitive nucleic acid assays, tremendous attentions have been focused on the development of various signal amplification strategies in recent years.[24–26] Deoxyribozymes, also called DNAzymes, are nucleic acid-based enzymatic molecules which exhibit excellent catalytic activities toward specific substrates.[27,28] Owing to the higher stability than protein enzyme in environment variations, such as temperature, pH, and ionic strength, DNAzymes have attracted considerable interest in the analysis of small molecules,[29,30] metal ions,[31,32] nucleic acids,[33,34] and proteins or enzymes.[35,36] As a typical kind of DNAzymes, Mg^{2+}-dependent DNAzyme generally consists of an enzymatic and a substrate sequence paired to each other. In the presence of Mg^{2+} as cofactors to perform the catalytic activity, the specific substrate sequence can be cleaved as expected.[37] During multiple turnovers, one Mg^{2+}-dependent DNAzyme can trigger the cleavage of a great number of substrates without losing its binding ability or activity, leading to the significant signal amplification for sensitive detection. For example,

Liu et al. constructed a dual-signal amplified fluorescence biosensor for DNA and avidin assays based on the catalytic hairpin DNA assembly-programmed active Mg^{2+}-dependent DNAzyme.[38] Moreover, the programmability of DNAzyme can be designed for a smart signal transducer to combine with other optical or electrochemical techniques. However, to date, few studies of this strategy for electrochemical DNA and miRNA detection have been reported.

In this paper, a novel electrochemical sensing strategy based on the molecular recognition of β-CDP initiated by the target-triggered assembly and cleavage reaction of Mg^{2+}-dependent DNAzyme was designed for sensitive detection of target DNA (Scheme 1). NRGO was synthesized by thermal annealing graphene oxide (GO) with melamine and then homogeneously dispersed in β-CDP aqueous solutions to produce NRGO/β-CDP nanocomposites, which were dropped onto the electrode surface to construct the sensing platform. In the absence of target, the formation of Mg^{2+}-dependent DNAzyme was blocked by the hybridization reaction of the stem domain of subunit DNA (S-1), and subsequently β-CDP on the electrode could not recognized the uncleaved hairpin probe (H-1) resulting from the principle of dimension matching (Figure S1 in the Supporting Information), leading to a weak current response. Upon the interaction of S-1 in the loop region with the target sequence, the hairpin structure of S-1 was opened, generating the active DNAzyme structure to catalyze the cleavage of H-1, due to the synergistic binding of H-1 in the presence of cofactor Mg^{2+}. After cleavage, the dual-labeled H-1 was divided into two single-stranded oligonucleotides, giving rise to an obvious increase of peak current by

the molecular recognition of β-CDP. Each activated DNAzyme could undergo a lot of recycles to achieve an amplified electrochemical signal for target. Therefore, the proposed biosensor displayed high sensitivity and selectivity for DNA detection. Moreover, the constructed sensing system was further used for the monitoring of miRNA with excellent performances, which may have promising applications in the construction of universal sensing platforms.

■ RESULTS AND DISCUSSION

Characterizations of β-CDP and NRGO. The solubility of β-CDP in water at room temperature was measured as 159.6g L^{-1}, which was almost 8.63 times greater than that of unmodified β-CD (18.5g L^{-1}). The high aqueous solubility of β-CDP could be ascribed to the disruption of intermolecular hydrogen bonding by the polymerization reaction, leading to an intense interaction between surrounding water molecules and β-CD.[19] The number average molecular weight (M_n) of β-CDP was estimated to be 44,897 g mol^{-1}. A typical ^1H NMR spectrum of β-CDP in D_2O was shown in Figure S2B, which was consistent with our previous work.[22] The broad proton peaks from 3.20 to 4.30 ppm were corresponded to the H2-H6a,b of β-CD unit and hydroxypropyl ether unit. Apart from the rest of signals, the H1 peaks of β-CD unit appeared at 4.97 ppm. The ^1H NMR analysis further applied to investigate the amount of β-CD units in the polymer with a molar β-CD : EP ratio of 1 : 7.

Compared to a sharp peak of graphite at 26.5°, the X-ray diffraction (XRD) pattern of GO displayed a relatively broad diffraction peak indexed as (002) at 10.3° with the increased inter-planar spacing of 8.58 Å (Figure 1A). The negative shift of diffraction

peak was attributed to the introduction of oxygen-containing functional groups to the layered structure. After thermal annealing and nitrogen doping of GO, a very broad profile at 26.1° appeared for NRGO, confirming that the resultant NRGO restored the graphite-like ordered structure after numerous oxygen-containing functional groups were removed from the nanosheets.[9]

The Raman spectrum of graphite exhibited an intense peak of the G band at 1581 cm^{-1} and a very weak peak of the D band at 1351 cm^{-1} (Figure 1B), which were related to the first-order scattering of the E_{2g} mode and a breathing mode of κ-point photons of A_{1g} symmetry, respectively.[39] The D band was ascribed to structural defects and partially disordered structures of the sp^2 domains, while the G band reflected the graphitization degree of the sp^2-hybridized carbon atoms. For GO and NRGO, the G bands were broadened and concomitant with the prominent D bands. The Raman intensity ratio of the D band to the G band (I_D/I_G) was significantly increased from 0.09 for graphite to 0.87 for GO (Table S1), confirming the decrease in size of the in-plane sp^2 domains on account of the ultrasonic exfoliation and extensive oxidation.[40] The higher intensity ratio I_D/I_G for NRGO could be attributed to the destruction of sp^2-hybridized carbon and the nitrogen doping in the graphene frameworks, leading to the increased defects after the thermal annealing GO with melamine.

X-ray photoelectron spectroscopy (XPS) measurements were tested to analyze the bonding configuration and elemental composition of the as-synthesized NRGO. The survey spectrum of GO displayed two distinct peaks of C 1s and O 1s (Figure 1C),

and the atomic concentration of oxygen was approximately 51.78 at% (Table S2). However, N 1s peak was observed for NRGO, concomitant with the remarkably decreased oxygen content (9.74 at%), which demonstrated that the great majority of oxygen-containing functional groups were effectively eliminated and nitrogen atoms from melamine were successfully introduced to the nanosheets.

In the high-resolution spectrum, the N 1s peak of NRGO was resolved into three components centered at 398.5, 400.1, and 401.5 eV, revealing the presence of pyridinic N, pyrrolic N, and graphitic N, respectively (Figure 1D). As illustrated in Figure 2A, pyridinic N and pyrrolic N can contribute to the π-conjugated systems with one p-electron and two p-electrons, whereas graphitic N is incorporated into the graphene layer to substitute the carbon atom in the hexagonal lattice.[41] These types of nitrogen atoms decorated the graphene planar structure to bring in the change of Fermi level, which could engender the doping effects and open the band gap of graphene.[42] Therefore, such doped nitrogen atoms regulated the electronic properties and improved the electrocatalytic behavior of graphene.

Similarly, the high-resolution C 1s spectrum of NRGO could be deconvoluted into four components (Figure 2B). The peak corresponding to the graphite-like sp^2 C (284.5 eV) was dominant, which revealed that the majority of carbon atoms in NRGO were arranged in a conjugated honeycomb lattice during the process of thermal annealing. Two peaks at 285.9 and 287.6 eV were assigned to the N-sp^2 C and N-sp^3 C, respectively, resulting from the substitutional doping of nitrogen atoms.[43–45] Moreover, the C 1s peak at 289.5 eV was indexed to the CO type bond by the physical

adsorption of oxygen on the surfaces.[45]

GO materials exhibited good solubility in water, and the resultant aqueous solution appeared brown (Figure 3A). After the reduction of GO at high temperature, water insoluble NRGO could be homogeneously and stably dispersed in β-CDP to produce black suspensions, due to the high water solubility of β-CDP. From the scanning electron microscope (SEM) and transmission electron microscope (TEM) images, NRGO nanosheets showed uniform laminar morphology like crumpled silk veil waves, and their edges were partially folded or scrolled (Figure 3B). After the introduction of β-CDP, the aggregation degree of NRGO nanosheets was obviously decreased with the almost transparent lamellar structures (Figure 3C,D).

Feasibility of the Sensing Strategy. Fluorescence spectra was applied to investigate the feasibility of the target-induced Mg^{2+}-dependent cleavage DNAzyme, in which the DNA probe (H-2) was modified with the fluorophore (FAM) and quencher (BHQ1) at its 5′ and 3′ termini, respectively (Figure S3). Before target was present, the hybridization of the stem domain of S-1 inhibited the formation of Mg^{2+}-dependent DNAzyme, and thus the uncleaved H-2 generated a low fluorescence background resulting from the quenching of FAM (Figure 4A). After target was added, the hairpin structure of S-1 was opened, thereby giving rise to the assembly of Mg^{2+}-dependent DNAzyme. The synergistic binding of H-2 to the DNAzyme triggered the cleavage of H-2 in the presence of Mg^{2+}, leading to an enhanced fluorescence signal by the separation of FAM and BHQ1. Furthermore, the fluorescence intensity was further increased with the increase of the reaction time. By

comprehensive consideration of the detection time and sensitivity, 1.5 h was selected for the subsequent measurements.

As a commonly used electrochemical testing technology, electrochemical impedance spectroscopy (EIS) has been extensively utilized to evaluate the interface characteristics of prepared electrodes. The impedance spectra generally included a semicircle portion at high frequencies and a linear section at low frequencies, representing the electron-transfer-limited and diffusion-limited process, respectively (Figure 4B). The diameter of the semicircle was equal to the charge transfer resistance (R_{ct}). A modified Randles' equivalent circuit (inset of Figure 4B), consisting of solution resistance (R_s) in series with parallel combination of constant phase element (CPE) and faradaic impedance (a series combination of R_{ct} and Warburg element (Z_w)), was utilized to fit the impedance data and extract the electrochemical parameters. The corresponding results were listed in Table S3. After the modification of GO on the glassy carbon electrode (GCE) surface, GO/GCE showed a large R_{ct} of 609.2 Ω compared to the bare GCE (187.1 Ω), which was ascribed to the inherently insulating property of GO as well as the electrostatic repulsion between the negatively charged GO and redox probes of $[Fe(CN)_6]^{3-/4-}$. In the case of RGO/β-CDP/GCE, the R_{ct} was significantly decreased to 127.6 Ω due to the excellent electron transfer property of RGO. When GCE was coated with NRGO/β-CDP nanocomposites, the R_{ct} was further decreased to 49.38 Ω, suggesting that the doping of nitrogen into RGO nanosheets further accelerated the electron transfer process from the redox probes to the electrode surface. These results demonstrated that the NRGO/β-CDP/GCE electrode could be

developed as an excellent detection platform for the subsequent nucleic acid analyses.

Optimization of Experimental Parameters. To achieve the superior electrochemical sensing performance in nucleic acid detections, experimental parameters such as the mass ratio of β-CDP to NRGO ($m_{\beta\text{-CDP}}/m_{\text{NRGO}}$) and the concentration of Mg^{2+} were investigated by the differential pulse voltammetry (DPV) method. The oxidation peak current enhanced with an increase of mass ratio $m_{\beta\text{-CDP}}/m_{\text{NRGO}}$ and reached a maximum at 3, and then decreased upon further increase of $m_{\beta\text{-CDP}}/m_{\text{NRGO}}$ to 5, indicating that high mass of β-CDP hindered the electron transfer due to its poor electronic conductivity (Figure S4A). Therefore, the mass ratio $m_{\beta\text{-CDP}}/m_{\text{NRGO}}$ of 3 was selected for subsequent experiments. When the Mg^{2+} concentration was more than 20 mM, no obvious peak current changes were observed, demonstrating that the cleavage reaction almost reached the maximum (Figure S4B). Thus, 20 mM Mg^{2+} was employed for further electrochemical determinations.

Analytical Performance of the Electrochemical Biosensor. By the smart combination of desirable host-guest recognition ability of β-CDP and the target-triggered cleavage reaction of Mg^{2+}-dependent DNAzyme, the constructed electrochemical biosensor was successfully used for the sensitive determination of DNA. As shown in Figure 5A, an oxidation peak appeared at 0.28 V (vs. SCE), and the current response increased proportionally with the increase of the target DNA concentration. It is obvious that NRGO/β-CDP/GCE showed a sensitive response to target DNA in comparison with GO/β-CDP/GCE and RGO/β-CDP/GCE (Figure S5). The increased peak current and decreased peak potential on NRGO/β-CDP/GCE

could be ascribed to the excellent electrocatalytic activity of NRGO. A desirable linear relationship between the peak current and the logarithm of DNA concentration was obtained on NRGO/β-CDP/GCE in the range from 10 fM to 1 nM with a regression equation of I (μA) = 0.665 + 0.045lg([DNA]/M) (R^2 = 0.9956), where I represents the peak current of the biosensor in the presence of target DNA (Figure 5B). The detection limit was calculated to be 3.2 fM at a signal-to-noise ratio of 3 (S/N = 3) using the following equation: [DNA] = $10^{((I - 0.665)/0.045)}$, where I is the sum of 3σ and the average current intensity of blank measurements (σ is the standard deviation of three parallel blank measurements). The linear range and detection limit were superior to the Mg^{2+}-dependent cleavage DNAzyme-based fluorescence DNA biosensor (Figure S6). For comparison, the analytical performances of different DNA biosensors with other signal amplification strategies were presented in Table S4. Obviously, the performances of our sensing strategy were better than most of the reported electrochemical biosensors for DNA determinations, which could be attributed to the high electrocatalytic activity of NRGO, superior recognition capability of β-CDP, and excellent cleavage reaction of Mg^{2+}-dependent DNAzyme.

Furthermore, the proposed sensing strategy could be demonstrated for target miRNA detection (Figure S7). When the concentration of miRNA was enhanced, the current response gradually increased and exhibited a good linear relationship with the logarithm of miRNA concentration ranging from 50 fM to 0.5 nM (Figure S8). The detection limit was estimated to be 18 fM (S/N = 3), which was much lower than 1 pM for the hybridization chain reaction-based homogenous electrochemical miRNA

biosensor[46] and 80 fM for the exonuclease I and G-quadruplex/hemin DNAzyme-based colorimetry sensing system for miRNA detection.[47]

Reproducibility, Stability, and Selectivity of Biosensor. The reproducibility of the developed sensing strategy was examined by the determination of 0.1 nM DNA in 0.1 M phosphate buffered solutions (pH 7.4, 0.1 M KCl). The relative standard deviation (RSD) for six parallel measurements on different electrodes was calculated to be 6.8%. When the electrode was stored in dark conditions at 4 °C for one month, over 90.2% of the original current response was retained. Thus, these results indicated that the proposed biosensor possessed satisfactory fabrication reproducibility and storage stability.

The selectivity of the constructed biosensor was further studied by comparing the current intensity of target to that of the other nucleic acid sequences including single-base and two-base mismatched DNA (Figure 6). Only the target could give rise to a significant current enhancement of the sensing system, whereas all other DNA sequences did not induce an obvious current increase, which demonstrated that the designed sensing platform exhibited high selectivity for target DNA to distinguish base mismatched sequences.

DNA Biosensing in Real Samples. The practical application of the developed analytical platform was also tested by the determination of target DNA in human serum samples. Prior to measurements, all the serum samples were diluted 10 times to avoid the decrease of DNA hybridization efficiency due to the highly concentrated tissue in serum. A good recovery in the range of 95.8%–103.4% with RSD (n = 5)

between 3.6% and 6.1% was obtained for the serum samples spiked with target DNA at different levels (Table S5). Thus, the fabricated electrochemical biosensors have potential applications for DNA detection in biological samples with acceptable accuracy.

■CONCLUSIONS

In summary, an enzyme-free electrochemical sensing system was developed to sensitively detect DNA and miRNA. The proposed strategy took advantages of the high electrocatalytic activity of NRGO, the excellent water solubility and recognition capability of β-CDP, and the target-initiated Mg^{2+}-assistant DNA recycling for signal amplification. Each target-triggered Mg^{2+}-dependent DNAzyme involved in the cleavage of a large number of hairpin probes, which could be recognized by β-CDP on the electrode, resulting in a significant enhancement of peak current in comparison with the absence of target. Therefore, the constructed biosensor possessed favorable performances with wide concentration ranges and low detection limits. Since other metal ion-dependent cleavage DNAzymes also can be employed in the proposed sensing system, the designed strategy opens a universal method for the preparation of electrochemical devices in bioassays and clinical diagnosis.

■ASSOCIATED CONTENT

Supporting Information

The Supporting Information is available free of charge on the ACS Publications website at http://pubs.acs.org.

Detailed experimental section, molecular model of Fc and cavity diameter of β-CD, chemical structure of β-CD unit and ^{1}H NMR spectrum of β-CDP, D and G peak positions, I_D/I_G, and atomic concentrations of NRGO, schematic representation of the target-induced cleavage of H-2, electrochemical parameters extracted from the EIS plots, optimization of $m_{\beta\text{-CDP}}/m_{NRGO}$ and Mg^{2+} concentration, DPV curves of different modified electrodes, fluorescence detection of target DNA, comparison of sensor performances, schematic illustration for miRNA detection, DPV detection of miRNA, and results for determination of DNA in serum samples (PDF)

■ AUTHOR INFORMATION

Corresponding Author

*E-mail: gwdiao@yzu.edu.cn. Fax: +86-514-87975244.

Notes

The authors declare no competing financial interest.

■ACKNOWLEDGMENTS

This work was financially supported by the National Natural Science Foundation of China (21511140282 and 21703199), Jiangsu Planned Projects for Postdoctoral Research Funds (1601138C), and a project funded by the Priority Academic Program Development of Jiangsu Higher Education Institutions.

■REFERENCES

[1] Sun, J. Y.; Gao, T.; Song, X. J.; Zhao, Y. F.; Lin, Y. W.; Wang, H. C.; Ma, D. L.; Chen, Y. B.; Xiang, W. F.; Wing, J.; Zhang, Y. F.; Liu, Z. F. Direct Growth of

High-Quality Graphene on High-kappa Dielectric $SrTiO_3$ Substrates. *J. Am. Chem. Soc.* **2014**, *136*, 6574−6577.

[2] Georgakilas, V.; Tiwari, J. N.; Kemp, K. C.; Perrnan, J. A.; Bourlinos, A. B.; Kim, K. S.; Zboril, R. Noncovalent Functionalization of Graphene and Graphene Oxide for Energy Materials, Biosensing, Catalytic, and Biomedical Applications. *Chem. Rev.* **2016**, *116*, 5464−5519.

[3] Allen, M. J.; Tung, V. C.; Kaner, R. B. Honeycomb Carbon: A Review of Graphene. *Chem. Rev.* **2010**, *110*, 132−145.

[4] Xu, J. T.; Wang, M.; Wickramaratne, N. P.; Jaroniec, M.; Dou, S. X.; Dai, L. M. High-Performance Sodium Ion Batteries Based on a 3D Anode from Nitrogen-Doped Graphene Foams. *Adv. Mater.* **2015**, *27*, 2042−2048.

[5] Liang, J.; Jiao, Y.; Jaroniec, M.; Qiao, S. Z. Sulfur and Nitrogen Dual-Doped Mesoporous Graphene Electrocatalyst for Oxygen Reduction with Synergistically Enhanced Performance. *Angew. Chem., Int. Ed.* **2012**, *51*, 11496−11500.

[6] Zhou, X. S.; Wan, L. J.; Guo, Y. G. Binding SnO_2 Nanocrystals in Nitrogen-Doped Graphene Sheets as Anode Materials for Lithium-Ion Batteries. *Adv. Mater.* **2013**, *25*, 2152−2157.

[7] Quan, B.; Yu, S. H.; Chung, D. Y.; Jin, A. H.; Park, J. H.; Sung, Y. E.; Piao, Y. Z. Single Source Precursor-based Solvothermal Synthesis of Heteroatom-Doped Graphene and Its Energy Storage and Conversion Applications. *Sci. Rep.* **2014**, *4*, 5639.

[8] Wang, X. R.; Li, X. L.; Zhang, L.; Yoon, Y.; Weber, P. K.; Wang, H. L.; Guo, J.; Dai, H. J. N-Doping of Graphene Through Electrothermal Reactions with Ammonia. *Science* **2009**, *324*, 768−771.

[9] Sheng, Z. H.; Shao, L.; Chen, J. J.; Bao, W. J.; Wang, F. B.; Xia, X. H.

Catalyst-Free Synthesis of Nitrogen-Doped Graphene via Thermal Annealing Graphite Oxide with Melamine and Its Excellent Electrocatalysis. *ACS Nano* **2011**, *5*, 4350−4358.

[10] Song, J. X.; Yu, Z. X.; Gordin, M. L.; Wang, D. H. Advanced Sulfur Cathode Enabled by Highly Crumpled Nitrogen-Doped Graphene Sheets for High-Energy-Density Lithium–Sulfur Batteries. *Nano Lett.* **2016**, *16*, 864−870.

[11] Zang, J. F.; Ryu, S.; Pugno, N.; Wang, Q. M.; Tu, Q.; Buehler, M. J.; Zhao, X. H. Multifunctionality and Control of the Crumpling and Unfolding of Large-Area Graphene. *Nat. Mater.* **2013**, *12*, 321−325.

[12] Liu, L. H.; Lerner, M. M.; Yan, M. D. Derivitization of Pristine Graphene with Well-Defined Chemical Functionalities. *Nano Lett.* **2010**, *10*, 3754−3756.

[13] Feng, L.; Liu, Y. W.; Tang, X. Y.; Piao, Y. M.; Chen, S. F.; Deng, S. L.; Xie, S. Y.; Wang, Y. H.; Zheng, L. S. Propagative Exfoliation of High Quality Graphene. *Chem. Mater.* **2013**, *25*, 4487−4496.

[14] Jana, M.; Khanra, P.; Murmu, N. C.; Samanta, P.; Lee, J. H.; Kuila, T. Covalent Surface Modification of Chemically Derived Graphene and Its Application as Supercapacitor Electrode Material. *Phys. Chem. Chem. Phys.* **2014**, *16*, 7618−7626.

[15] Xu, Y. X.; Bai, H.; Lu, G. W.; Li, C.; Shi, G. Q. Flexible Graphene Films via the Filtration of Water-Soluble Noncovalent Functionalized Graphene Sheets. *J. Am. Chem. Soc.* **2008**, *130*, 5856−5857.

[16] Lu, X. B.; Wang, X.; Jin, J.; Zhang, Q.; Chen, J. P. Electrochemical Biosensing Platform Based on Amino Acid Ionic Liquid Functionalized Graphene for Ultrasensitive Biosensing Applications. *Biosens. Bioelectron.* **2014**, *62*, 134−139.

[17] Xu, X. J.; Ou, D. X.; Luo, X. L.; Chen, J.; Lu, J. J.; Zhan, H. B.; Dong, Y. Q.; Qin,

J. G.; Li, Z. Water-Soluble Graphene Sheets with Large Optical Limiting Response via Non-Covalent Functionalization with Polyacetylenes. *J. Mater. Chem.* **2012**, *22*, 22624−22630.

[18] Yu, P.; Zhang, X. H.; Zhou, J. W.; Xiong, E. H.; Li, X. Y.; Chen, J. H. Smart Protein Biogate as a Mediator to Regulate Competitive Host-Guest Interaction for Sensitive Ratiometric Electrochemical Assay of Prion. *Sci. Rep.* **2015**, *5*, 16015.

[19] Li, J. S.; Xiao, H. N.; Li, J. H.; Zhong, Y. P. Drug Carrier Systems Based on Water-Soluble Cationic β-Cyclodextrin Polymers. *Int. J. Pharmaceut.* **2004**, *278*, 329−342.

[20] Guo, Y. J.; Guo, S. J.; Ren, J. T.; Zhai, Y. M.; Dong, S. J.; Wang, E. K. Cyclodextrin Functionalized Graphene Nanosheets with High Supramolecular Recognition Capability: Synthesis and Host−Guest Inclusion for Enhanced Electrochemical Performance. *ACS Nano* **2010**, *4*, 4001−4010.

[21] Yang, L.; Fan, S. M.; Deng, G. G.; Li, Y. C.; Ran, X.; Zhao, H.; Li, C. P. Bridged β-Cyclodextrin-Functionalized MWCNT with Higher Supramolecular Recognition Capability: The Simultaneous Electrochemical Determination of Three Phenols. *Biosens. Bioelectron.* **2015**, *68*, 617−625.

[22] Zhang, W.; Chen, M.; Diao, G. W. Preparation and Electrochemical Behavior of Water-Soluble Inclusion Complex of Ferrocene with β-Cyclodextrin Polymer. *Electrochim. Acta* **2011**, *56*, 5129−5136.

[23] Alsbaiee, A.; Smith, B. J.; Xiao, L. L.; Ling, Y. H.; Helbling, D. E.; Dichtel, W. R. Rapid Removal of Organic Micropollutants from Water by a Porous β-Cyclodextrin Polymer. *Nature* **2016**, *529*, 190−194.

[24] Zhao, Z. H.; Chen, S. X.; Wang, J. B.; Su, J.; Xu, J. Q.; Mathur, S.; Fan, C. H.; Song, S. P. Nuclease-Free Target Recycling Signal Amplification for

Ultrasensitive Multiplexing DNA Biosensing. *Biosens. Bioelectron.* **2017**, *94*, 605−608.

[25] Shi, X. M.; Fan, G. C.; Shen, Q. M.; Zhu, J. J. Photoelectrochemical DNA Biosensor Based on Dual-Signal Amplification Strategy Integrating Inorganic−Organic Nanocomposites Sensitization with λ-Exonuclease-Assisted Target Recycling. *ACS Appl. Mater. Interfaces* **2016**, *8*, 35091−35098.

[26] Wang, X. Y.; Chen, F.; Zhang, D. X.; Zhao, Y.; Wei, J.; Wang, L. H.; Song, S. P.; Fan, C. H.; Zhao, Y. X. Single Copy-Sensitive Electrochemical Assay for Circulating Methylated DNA in Clinical Samples with Ultrahigh Specificity Based on A Sequential Discrimination–Amplification Strategy. *Chem. Sci.* **2017**, *8*, 4764−4770.

[27] Wang, F.; Lu, C. H.; Willner, I. From Cascaded Catalytic Nucleic Acids to Enzyme-DNA Nanostructures: Controlling Reactivity, Sensing, Logic Operations, and Assembly of Complex Structures. *Chem. Rev.* **2014**, *114*, 2881−2941.

[28] Xia, H.; Li, L. L.; Yin, Z. Y.; Hou, X. D.; Zhu, J. J. Biobar-Coded Gold Nanoparticles and DNAzyme-Based Dual Signal Amplification Strategy for Ultrasensitive Detection of Protein by Electrochemiluminescence. *ACS Appl. Mater. Interfaces* **2015**, *7*, 696−703.

[29] Guo, Y. S.; Liu, J.; Yang, G. X.; Sun, X. F.; Chen, H. Y.; Xu, J. J. Multiple Turnovers of DNAzyme for Amplified Detection of ATP and Reduced Thiol in Cell Homogenates. *Chem. Commun.* **2015**, *51*, 862−865.

[30] Liao, S. Z.; Ding, H. Z.; Wu, Y.; Wu, Z. Y.; Shen, G. L.; Yu, R. Q. Label-Free Liquid Crystal Biosensor for L-Histidine: A DNAzyme-Based Platform for Small Molecule Assay. *Biosens. Bioelectron.* **2016**, *79*, 650−655.

[31] Wen, Y. Q.; Peng, C.; Li, D.; Zhuo, L.; He, S. J.; Wang, L. H.; Huang, Q.; Xu, Q.

H.; Fan, C. H. Metal Ion-Modulated Graphene-DNAzyme Interactions: Design of A Nanoprobe for Fluorescent Detection of Lead(II) Ions with High Sensitivity, Selectivity and Tunable Dynamic Range. *Chem. Commun*. **2011**, *47*, 6278−6280.

[32] Li, X.; Xie, J. Q.; Jiang, B. Y.; Yuan, R.; Xiang, Y. Metallo-Toehold-Activated Catalytic Hairpin Assembly Formation of Three-Way DNAzyme Junctions for Amplified Fluorescent Detection of Hg^{2+}. *ACS Appl. Mater. Interfaces* **2017**, *9*, 5733−5738.

[33] Li, J.; Zhao, J. J.; Li, S. T.; Zhang, L. L.; Huang, Y.; Zhao, S. L.; Liu, Y. M. Electrophoresis Separation Assisted G-Quadruplex DNAzyme-Based Chemiluminescence Signal Amplification Strategy on a Microchip Platform for Highly Sensitive Detection of MicroRNA. *Chem. Commun.* **2016**, *52*, 12806−12809.

[34] Nakayama, S.; Sintim, H. O. Colorimetric Split G-Quadruplex Probes for Nucleic Acid Sensing: Improving Reconstituted DNAzyme's Catalytic Efficiency via Probe Remodeling. *J. Am. Chem. Soc.* **2009**, *131*, 10320−10333.

[35] Tang, L. H.; Liu, Y.; Ali, M. M.; Kang, D. K.; Zhao, W. A.; Li, J. H. Colorimetric and Ultrasensitive Bioassay Based on a Dual-Amplification System Using Aptamer and DNAzyme. *Anal. Chem.* **2012**, *84*, 4711−4717.

[36] Yang, J. M.; Dou, B. T.; Yuan, R.; Xiang, Y. Proximity Binding and Metal Ion-Dependent DNAzyme Cyclic Amplification-Integrated Aptasensor for Label-Free and Sensitive Electrochemical Detection of Thrombin. *Anal. Chem.* **2016**, *88*, 8218−8223.

[37] Wang, Y.; Zhang, J. Y.; Zhu, L. L.; Lu, L. L.; Feng, C. C.; Wang, F. Y.; Xu, Z. A.; Zhang, W. Activation of Mg^{2+}-Dependent DNAzymes Based on AP Site-Containing Triplex for Specific Melamine Recognition. *Analyst* **2015**, *140*,

7508−7512.

[38] Liu, S. F.; Cheng, C. B.; Gong, H. W.; Wang, L. Programmable Mg^{2+}-Dependent DNAzyme Switch by the Catalytic Hairpin DNA Assembly for Dual-Signal Amplification toward Homogeneous Analysis of Protein and DNA. *Chem. Commun.* **2015**, *51*, 7364−7367.

[39] Zhu, C. Z.; Guo, S. J.; Fang, Y. X.; Dong, S. J. Reducing Sugar: New Functional Molecules for the Green Synthesis of Graphene Nanosheets. *ACS Nano* **2010**, *4*, 2429−2437.

[40] Stankovich, S.; Dikin, D. A.; Piner, R. D.; Kohlhaas, K. A.; Kleinhammes, A.; Jia, Y. Y.; Wu, Y.; Nguyen, S. T.; Ruoff, R. S. Synthesis of Graphene-Based Nanosheets via Chemical Reduction of Exfoliated Graphite Oxide. *Carbon* **2007**, *45*, 1558−1565.

[41] Wang, H. B.; Xie, M. S.; Thia, L.; Fisher, A.; Wang, X. Strategies on the Design of Nitrogen-Doped Graphene. *J. Phys. Chem. Lett.* **2014**, *5*, 119−125.

[42] Wang, Y.; Shao, Y. Y.; Matson, D. W.; Li, J. H.; Lin, Y. H. Nitrogen-Doped Graphene and Its Application in Electrochemical Biosensing. *ACS Nano* **2010**, *4*, 1790−1798.

[43] Wei, D. C.; Liu, Y. Q.; Wang, Y.; Zhang, H. L.; Huang, L. P.; Yu, G. Synthesis of N-Doped Graphene by Chemical Vapor Deposition and Its Electrical Properties. *Nano Lett.* **2009**, *9*, 1752−1758.

[44] Reddy, A. L. M.; Srivastava, A.; Gowda, S. R.; Gullapalli, H.; Dubey, M.; Ajayan, P. M. Synthesis Of Nitrogen-Doped Graphene Films For Lithium Battery Application. *ACS Nano* **2010**, *4*, 6337−6342.

[45] Zhang, C. H.; Fu, L.; Liu, N.; Liu, M. H.; Wang, Y. Y.; Liu, Z. F. Synthesis of Nitrogen-Doped Graphene Using Embedded Carbon and Nitrogen Sources. *Adv.*

Mater. **2011**, *23*, 1020−1024.

[46] Hou, T.; Li, W.; Liu, X. J.; Li, F. Label-Free and Enzyme-Free Homogeneous Electrochemical Biosensing Strategy Based on Hybridization Chain Reaction: A Facile, Sensitive, and Highly Specific MicroRNA Assay. *Anal. Chem.* **2015**, *87*, 11368−11374.

[47] Li, S. Y.; Li, R.; Dong, M. M.; Zhang, L. Y.; Jiang, Y.; Chen, L. J.; Qi, W.; Wang, H. High-Throughput, Selective, and Sensitive Colorimetry for Free MicroRNAs in Blood via Exonuclease I Digestion and Hemin-G-Quadruplex Catalysis Reactions Based on A "Self-Cleaning" Functionalized Microarray. *Sens. Actuators B* **2016**, *222*, 198−204.

Figure captions:

Scheme 1. Schematic Illustration of the Electrochemical DNA Biosensor Based on the Host-Guest Interaction and Mg^{2+}-Assistant DNA Recycling

Figure 1. (A) XRD patterns and (B) Raman spectra of (a) graphite, (b) GO, and (c) NRGO. (C) XPS spectra of (a) GO and (b) NRGO. (D) High-resolution XPS spectra of NRGO in the N 1s region.

Figure 2. (A) Schematic structure of NRGO. (B) High-resolution XPS spectra of NRGO in the C 1s region.

Figure 3. (A) Photographs of (a) GO and (b) NRGO in aqueous solution, and (c) NRGO in β-CDP solution. (B) SEM image of NRGO. TEM images of NRGO in (C) aqueous solution and (D) β-CDP solution.

Figure 4. (A) Fluorescence spectra of H-2 at λ_{ex} of 495 nm after incubated with (a) DNAzyme buffer, (b-g) DNAzyme buffer containing the mixture of (b) S-1 and S-2, (c-g) S-1, S-2 and target DNA for (c) 0.5 h, (d) 1.0 h, (e) 1.5 h, (f) 2.0 h, (g) 2.5 h. (B) EIS Nyquist plots of (a) bare GCE, (b) GO/GCE, (c) RGO/β-CDP/GCE, and (d) NRGO/β-CDP/GCE in 0.1 M KCl solution containing a 5 mM $[Fe(CN)_6]^{3-/4-}$ mixture (1:1) with the applied potential of 0.18 V (vs. SCE). Inset: a modified Randles' equivalent circuit model applied to fit the impedance data.

Figure 5. (A) DPV responses of the proposed biosensor toward 10, 100, 1000, 1.0×10^4, 1.0×10^5, 1.0×10^6, and 1.0×10^7 fM DNA (from a to g). (B) Calibration curve of the peak current versus the logarithm of target DNA concentration. The error bars represent standard deviations for five tests.

Figure 6. Selectivity of the fabricated electrochemical biosensor toward 0.1 nM of (a) complementary target DNA, (b) single-base mismatched DNA, (c) two-base mismatched DNA, and (d) blank. The error bars represent standard deviations for five

tests.

Scheme 1

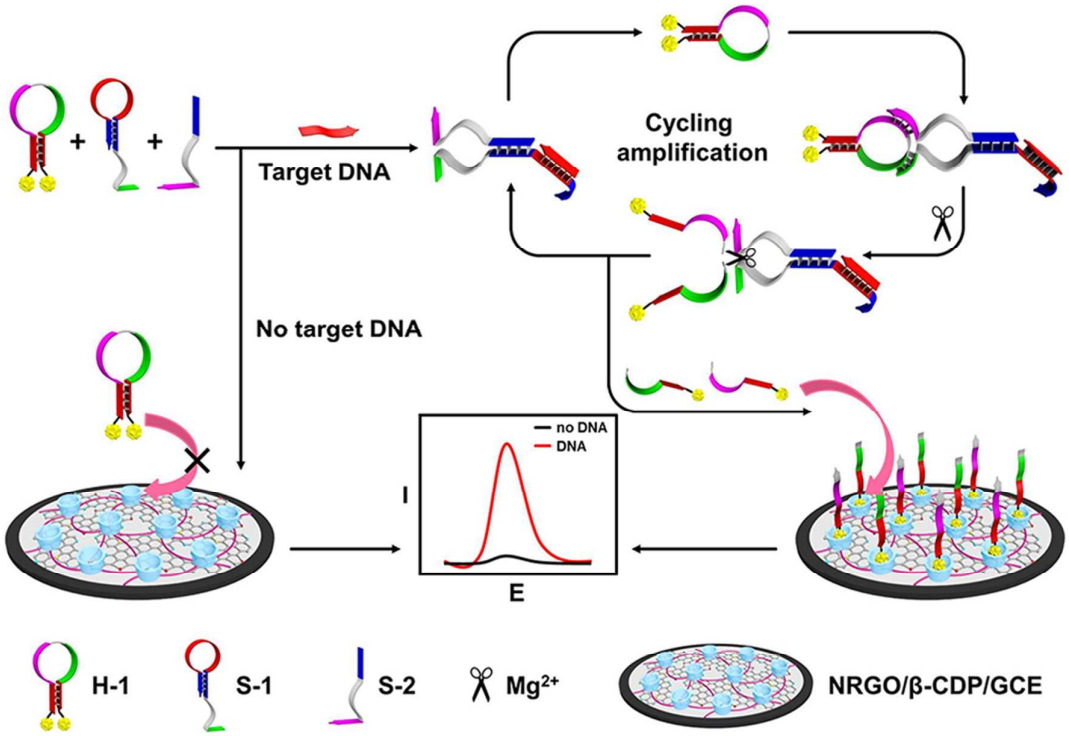
Target DNA
Cycling amplification
No target DNA
no DNA
DNA
I
E
H-1
S-1
S-2
Mg2+
NRGO/β-CDP/GCE

Figure 1

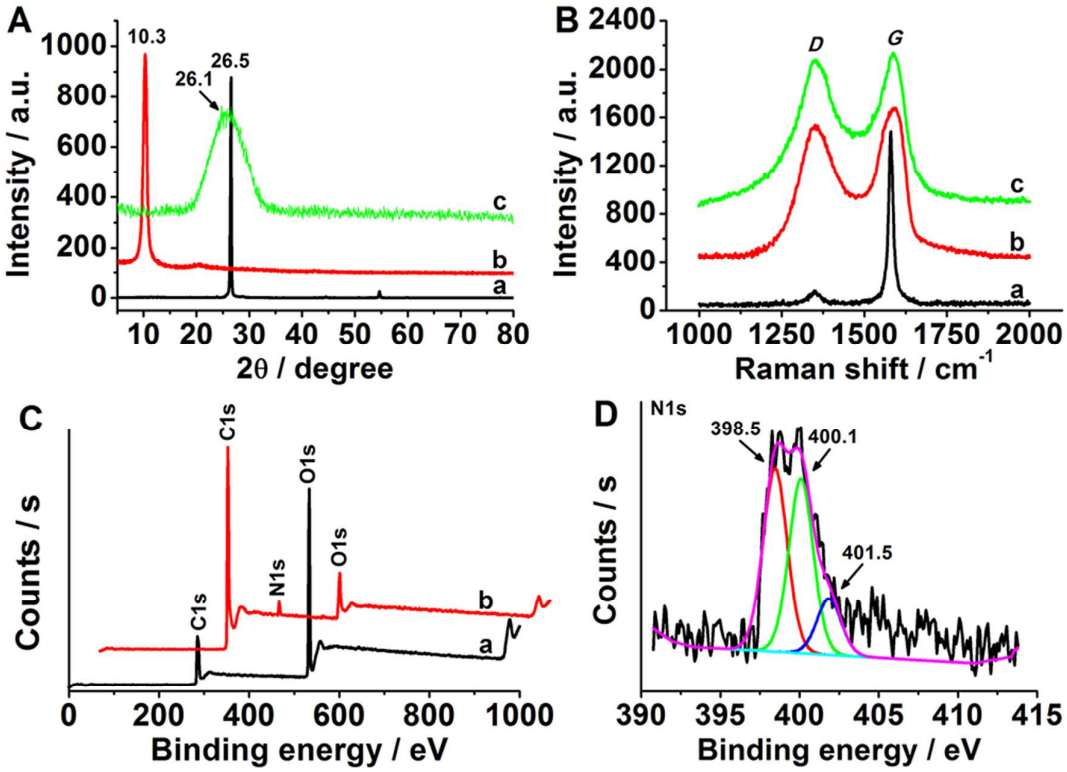
A
Intensity / a.u.
2θ / degree
10.3
26.1
26.5
a
b
c
B
Intensity / a.u.
Raman shift / cm-1
D
G
a
b
c
C
Counts / s
Binding energy / eV
C1s
N1s
O1s
O1s
C1s
a
b
D
Counts / s
Binding energy / eV
N1s
398.5
400.1
401.5

Figure 2

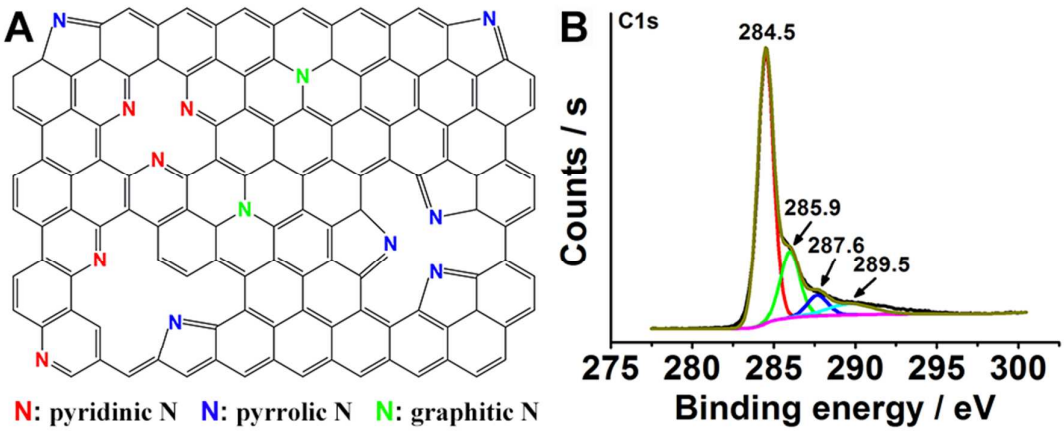
A
N
N
N
N
N
N
N
N
N
N
N
N
N
N: pyridinic N
N: pyrrolic N
N: graphitic N
B
C1s
284.5
285.9
287.6
289.5
Counts / s
275
280
285
290
295
300
Binding energy / eV

Figure 3

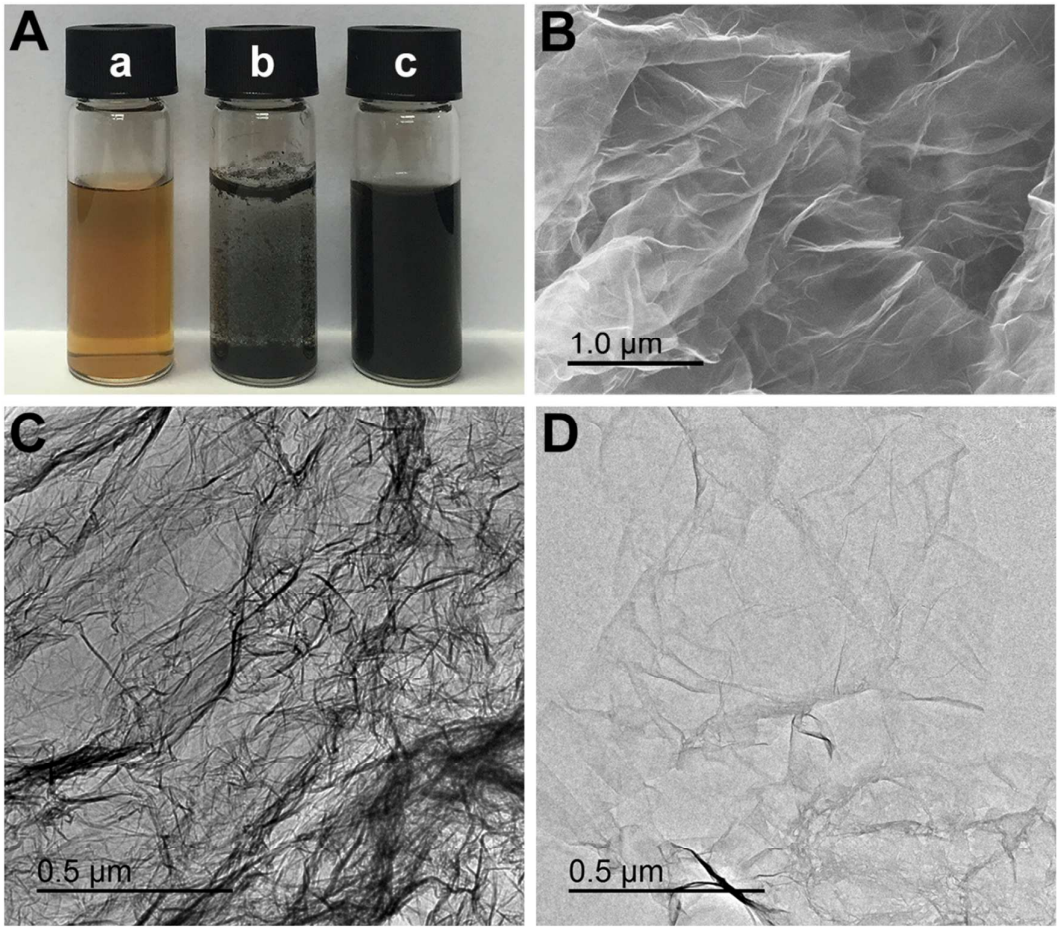

Figure 4

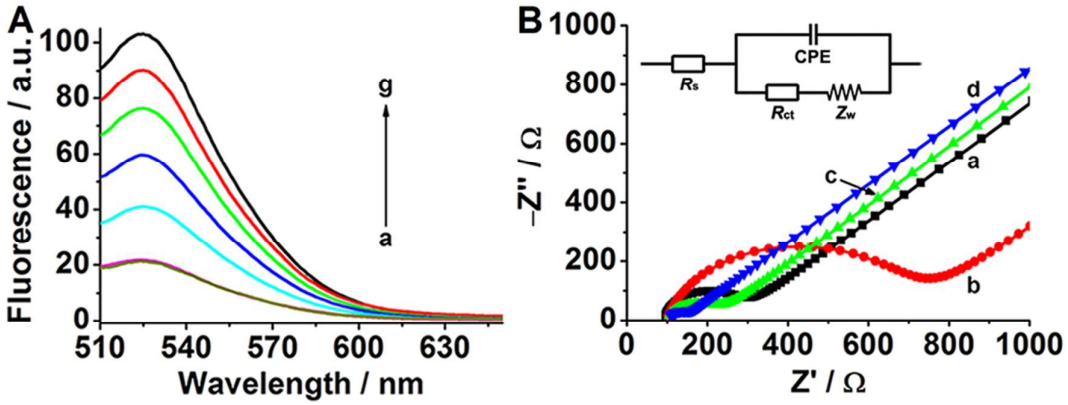
A
Fluorescence / a.u.
100
80
60
40
20
0
510
540
570
600
630
Wavelength / nm
g
a
B
1000
800
600
400
200
0
0
200
400
600
800
1000
-Z'' / Ω
Z' / Ω
CPE
Rs
Rct
Zw
d
a
c
b

Figure 5

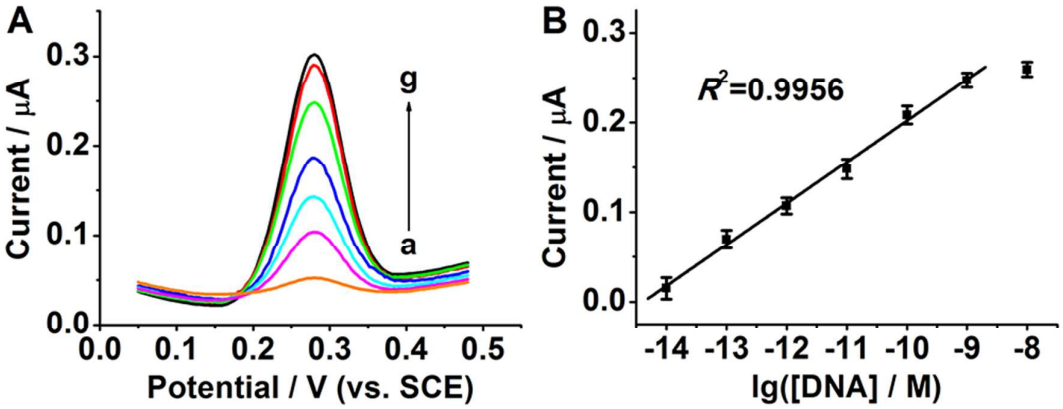
A
Current / μA
0.3
0.2
0.1
0.0
g
a
0.0 0.1 0.2 0.3 0.4 0.5
Potential / V (vs. SCE)
B
Current / μA
0.3
0.2
0.1
0.0
R²=0.9956
-14 -13 -12 -11 -10 -9 -8
lg([DNA] / M)

Figure 6

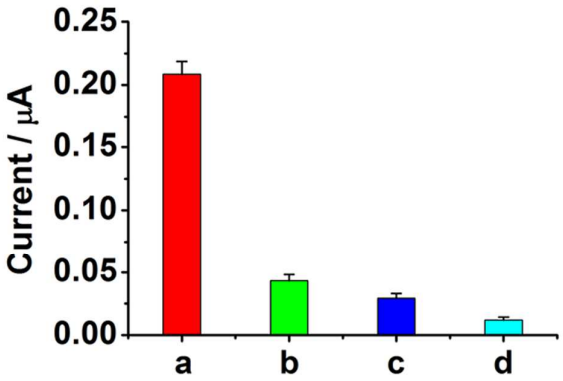

Table of Contents